Soft and Hard Magnetic Properties of Nanocrystalline Fe-M-B (M=Zr, Nd) Base Alloys Containing Intergranular Amorphous Phase

Sci. Rep. RITU A42 (1996) pp. 143-156
No. 1, March 1996

Soft and Hard Magnetic Properties of Nanocrystalline Fe-M-B (M=Zr, Nd) Base Alloys Containing Intergranular Amorphous Phase*

A. Inoue[1], A. Takeuchi[1], A. Makino[2] and T. Masumoto[1]
[1]*Institute for Materials Research, Tohoku University, Sendai 980-77, Japan*
[2]*Nagaoka Branch, Central Research Laboratory, Alps Electric Co., Ltd., Nagaoka 940, Japan*
(Received January 10, 1996)

This paper reviews our recent results of the soft and hard magnetic properties of nanocrystalline Fe-rich Fe-M-B (M=Nd or Zr) base alloys containing an intergranular amorphous phase. Based on the previous results that the soft magnetic alloys in Fe-Si-B-Nb-Cu and Fe-Zr-B systems do not have zero magnetostriction (λ_s), the effect of the additional Al or Si on the λ_s and magnetic properties was examined for the nanocrystalline Fe-Zr-B-Al and Fe-Zr-B-Si alloys. The soft magnetic properties of high Bs above 1.5 T and high μ_e above 1.5×10^4 combined with zero λ_s were obtained for the $Fe_{88}Zr_7B_3Al_2$ and $Fe_{86}Zr_7B_3Si_4$ alloys annealed for 3.6 ks in the annealing temperature (Ta) range of 823 to 923 K. This is in contrast to the previous result that the good soft magnetic properties of the nanocrystalline $Fe_{90}Zr_7B_3$ alloy are obtained in the narrow Ta range around 923 K. The remarkable extension of the Ta range seems to be attributed to the zero λ_s. The replacement of Zr by Nd in the $Fe_{90}M_7B_3$ alloys was found to cause rather good hard magnetic properties of 1.3 T for Br, 260 kA/m for iHc and 146 kJ/m^3 for $(BH)_{max}$ in a triplex nanostructure of bcc-Fe with a size of 20 nm, tetragonal $Fe_{14}Nd_2B$ with a size of 15 nm and intergranular amorphous phase with a thickness of 5 to 10 nm. The hard magnetic properties are obtained for the nanostructure containing 80 % soft magnetic phases and 20 % $Fe_{14}Nd_2B$ in volume. The notable result is presumably due to the effective action of the intergranular amorphous network phase which can act as a resistance against the nucleation of the reversion of magnetic domain walls leading to the increase in iHc as well as an exchange magnetic coupling medium between bcc-Fe and bcc-Fe or tetragonal $Fe_{14}Nd_2B$ phases leading to the high Br. This presumption is also supported from the result that no good hard magnetic properties are obtained for the over annealed sample without intergranular amorphous phase as well as for the use of the sample which does not consist of a mostly single amorphous phase in the as-quenched state. Thus, the soft and hard magnetic properties for the Fe-M-B alloys are obtained only in the optimal nanostructures. The fabrication of a new nanostructure is expected to cause the appearance of other function properties even at compositions where no useful properties have not been obtained.

KEYWORDS: soft magnetic properties, hard magnetic properties, iron base alloys, amorphous phase, nanocrystallization

1. Introduction

Recently, there has been great attention to nanocrystalline alloys. The increasing attention is mainly due to the appearance of high functional properties which are not obtained for amorphous single phase alloys as well as for conventionally controlled structure alloys even at the same alloy compositions. As the functional properties which have been reported for nanocrystalline alloys, one can list up high mechanical strength, soft magnetic properties, hard magnetic properties, highly sensitive magnetostriction and high catalytic properties[1]. It is to be noticed that these functional properties are achieved for the nanocrystalline alloys obtained by crystallization of a rapidly solidified amorphous phase, though many techniques leading to the formation of the nanocrystalline phase have been reported[2]. When we focus on the nanocrystalline magnetic alloys, nanocrystalline bcc alloys in Fe-Si-B-Nb-Cu[3] and Fe-M-B (M=Zr, Hf or Nb)[4] systems are known to exhibit good soft magnetic properties. In particular, the Fe-M-B alloys have the best combination of high saturation magnetization (Bs) of about 1.7 T and high permeability (μ_e) exceeding 10^5 at 1 kHz. In addition to the soft magnetic properties, the replacement of Zr by Nd in the Fe-rich $Fe_{90}M_7B_3$ alloys has more recently been found to cause the appearance of good hard magnetic properties[5], though no hard magnetic properties are obtained for the same alloy prepared by the conventional preparation method. The appearance of the soft and hard magnetic properties for the same alloy series of $Fe_{90}M_7B_3$ (M=Zr, Hf, Nb or Nd) is particularly interest for basic science and engineering materials. Furthermore, when attention is paid to the soft magnetic alloys, the addition of a small amount of Al or Si to the Fe-M-B (M=Zr or Hf) alloys has been found[6] to be effective for the achievement of good soft magnetic properties in a much wider annealing temperature range. This has been attributed to the attainment of nearly zero magnetostriction as well as to the increase in the critical sample thickness for glass formation in comparison with that for the Fe-M-B amorphous alloys. This paper is intended to review our recent results on the formation of the nanostructure including an intergranular amorphous phase for the Fe-M-B (M=Zr or Nd) based alloys by crystallization of their amorphous phase and the soft and hard magnetic properties of the resulting nanostructure alloys.

2. Nanocrystalline Soft Magnetic Alloys in Fe-Zr-B-Al and Fe-Zr-B-Si Systems[6,7]

Before the data on the quaternary alloys containing Al or Si are presented, it is important to introduce very briefly the soft magnetic properties for the nanocrystalline Fe-Zr-B

*IMR, Report No. 2021

ternary alloy[8] because the addition of Al or Si has been intended to improve the soft magnetic properties of the ternary alloy. The $Fe_{90}Zr_7B_3$ amorphous alloy crystallizes through two stages consisting of the precipitations of a bcc-Fe phase as a primary phase and a cubic Fe_3Zr phase as a secondary phase from the remaining amorphous phase. The sample heated to the temperature just below the second exothermic reaction consists of a bcc structure with a grain size of 15 to 20 nm. The nanoscale bcc alloy exhibits excellent soft magnetic properties of high μ_e reaching 10^5 at 1 kHz combined with high Bs of 1.7 T. In comparison with the data on the other conventional soft magnetic alloys shown in Fig. 1, one can notice that the nanoscale bcc Fe-M-B alloys have the best combined soft magnetic properties of high μe and high Bs. Figure 2 summarizes the μ_e, Bs, saturated magnetostriction (λ_s) and crystallized structure as a function of Ta for the nanoscale bcc $Fe_{90}Zr_7B_3$ and $Fe_{90}Hf_7B_3$ alloys[8]. The best soft magnetic properties are obtained in a narrow Ta range around 923 K. However, it is seen that the bcc alloys exhibiting the best soft magnetic properties do not have zero λ_s and possess negative λ_s values. It is therefore expected that the modification of λ_s to nearly zero value causes the further improvement of the soft magnetic properties.

Table 1 summarizes the solute concentrations of the bcc phase and magnetostriction for typical soft magnetic Fe-Si-B-Nb-Cu and Fe-M-B (M=Zr or Hf) alloys. The bcc-Fe phase in the Fe-Si-B-Nb-Cu alloy contains about 20 to 25 at% Si and has positive λ_s, while the bcc-Fe phase in the Fe-Zr-B soft magnetic alloys is a nearly pure Fe and the λ_s is negative. Consequently, with the aim of fabricating a nanoscale bcc phase with a nearly zero λ_s, we tried to fabricate bcc Fe(Al), Fe(Si) and Fe(Al,Si) solid solutions by adding a small amount of Al or Si. The resulting bcc solid solutions are expected to have nearly zero λ_s, decreased magnetic anisotropy and high electrical resistivity which are appropriate for further improvement of soft magnetic properties.

An amorphous phase is formed by melt spinning in the wide composition ranges up to 20 at% Al or Si for the alloy series of $Fe_{90-x}Zr_7B_3Al_x$ and $Fe_{90-x}Zr_7B_3Si_x$. The amorphous alloys containing 2 %Al or 4 %Si also crystallize through two stages. The first stage is due to the precipitation of the bcc-Fe phase and the second stage corresponds to the precipitation of a cubic Fe_3Zr phase from the remaining amorphous phase. As an example, Fig. 3 shows the X-ray diffraction patterns of the $Fe_{88}Zr_7B_3Al_2$ amorphous alloy heated to various temperatures. The samples heated to 823 and 923 K consist only of a bcc-phase and the bcc phase is

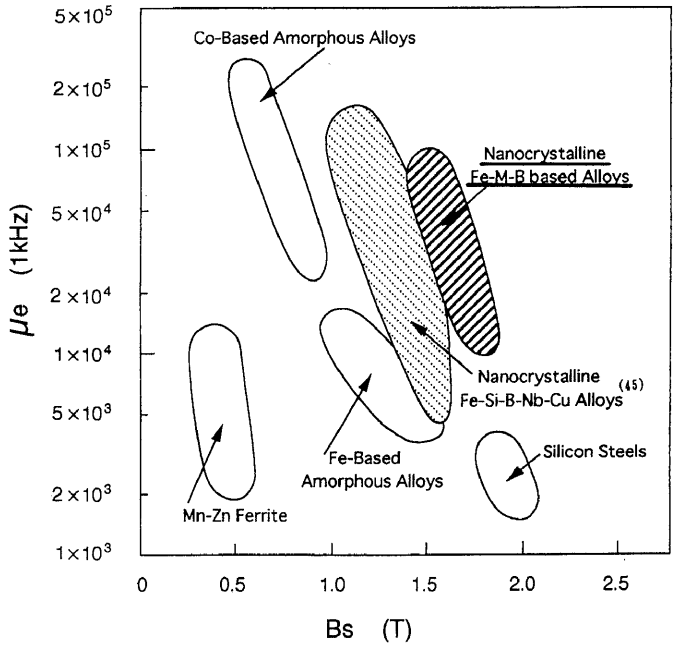

Fig. 1 Correlation between effective permeability (μ_e) at 1 kHz and saturation magnetization (Bs) for nanocrystalline Fe-M-B (M=Zr, Hf, Nb) base alloys. The data on the conventional soft magnetic alloys are also shown for comparison.

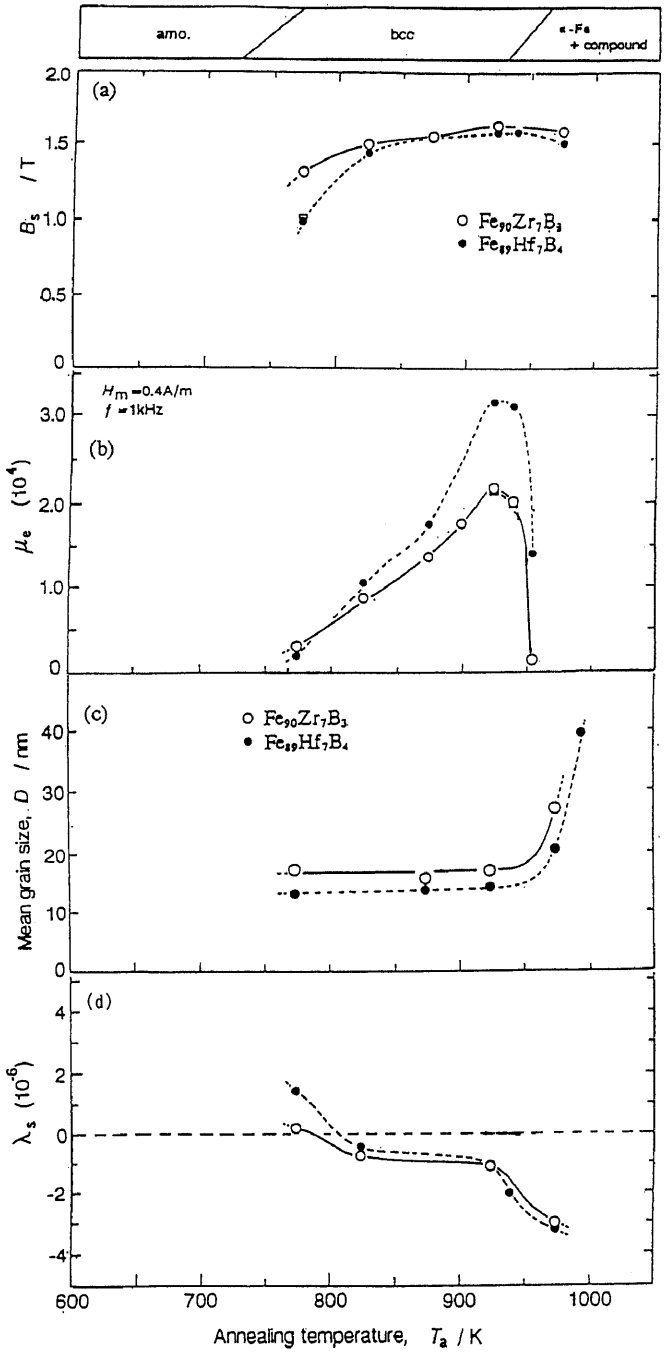

Fig. 2 Changes in the structure, Bs, μ_e, mean grain size (D) and λ_s as a function of Ta for $Fe_{90}Zr_7B_3$ and $Fe_{89}Hf_7B_4$ amorphous alloys.

recognized to be formed in a very wide temperature interval of about 200 K. The similar wide temperature interval of about 200 K was also recognized for the $Fe_{86}Zr_7Si_4B_3$ alloy. From the bright-field electron micrographs and selected-area electron diffraction patterns taken from the bcc $Fe_{88}Zr_7B_3Al_2$ and $Fe_{86}Zr_7Si_4B_3$ alloys, the bcc phase consists of equiaxed nanograins with a grain size of about 15 to 20 nm.

Table 1 Constituent phases and magnetostriction of typical nanocrystalline soft magnetic alloys.

Structure and Magnetostriction of Typical Nanocrystalline Soft Magnetic Alloys
1. Fe-Si-B-Nb-Cu Soft Magnetic Alloys
Nanostructure: bcc-Fe(Si) + amorphous
Si content: 20-25 at%
Positive magnetostriction
2. Fe-Zr-B Soft Magnetic Alloys
Nanostructure: a-Fe + amorphous
Negative magnetostriction
3. Fe-Zr-Al-B, Fe-Zr-Si-B and Fe-Zr-Al-Si-B Alloys
Nanostructure: amorphous plus bcc-Fe(Al), bcc-Fe(Si) or bcc-Fe(Al,Si) containing a small amount of Al and/or Si
Nearly zero magnetostriction
Decrease of magnetic anisotropy
Increase of electrical resistivity

The λ_s values of the nanoscale bcc Fe-Zr-B-Al and Fe-Zr-B-Si alloys are plotted as a function of Al or Si content in Figs. 4 and 5, respectively, together with the data

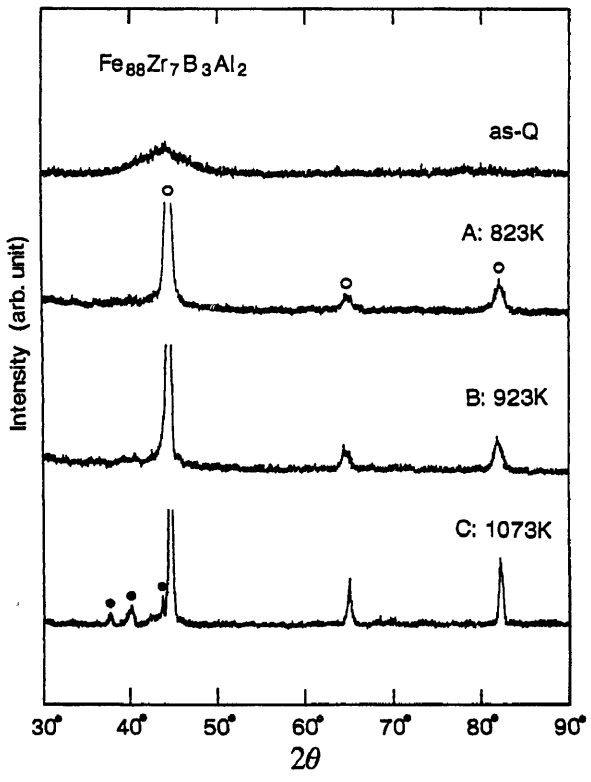

Fig. 3 X-ray diffraction patterns of the amorphous $Fe_{88}Zr_7B_3Al_2$ alloy annealed for 3.6 ks at 823, 923 and 1073 K.

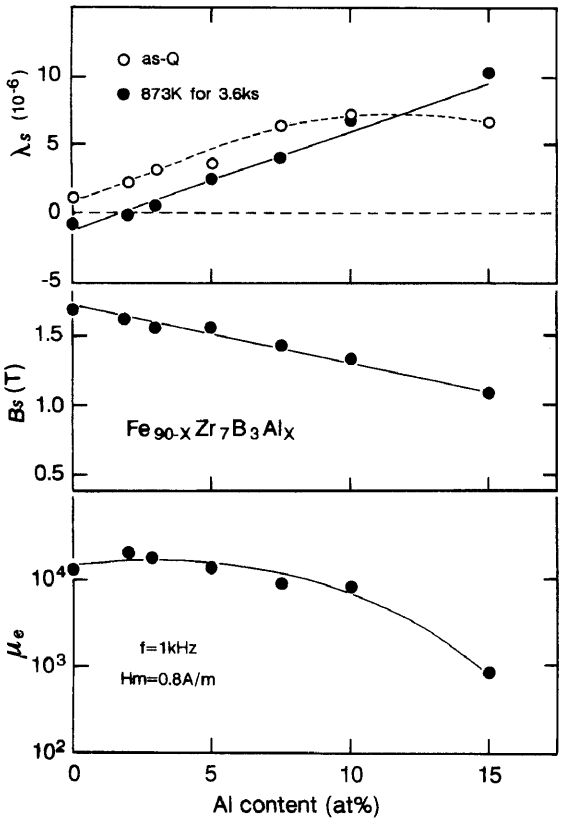

Fig. 4 Changes in λ_s, Bs and μ_e as a function of Al content for the nanocrystalline $Fe_{90-x}Zr_7B_3Al_x$ alloys annealed for 3.6 ks at 873 K. The data on λ_s in the as-quenched state are also shown for comparison.

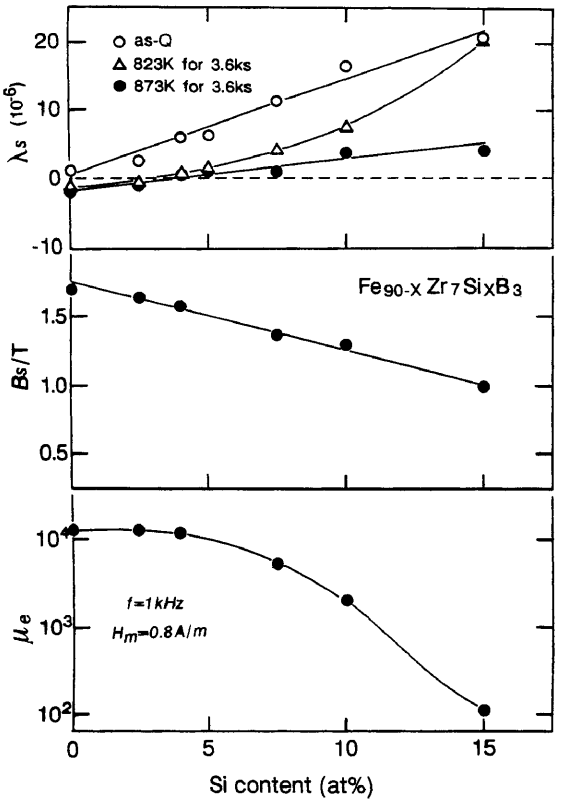

Fig. 5 Changes in λ_s, Bs and μ_e as a function of Si content for the nanocrystalline $Fe_{90-x}Zr_7B_3Si_x$ alloys annealed for 3.6 ks at 823 and 873 K. The data on λ_s in the as-quenched state are also shown for comparison.

on the Bs and μ_e. The λ_s value is negative for the bcc Fe-Zr-B ternary alloy and increases almost linearly with increasing Al or Si content. As a result, a nearly zero λ_s value is obtained in the vicinity of 2 at% Al or 4 at% Si, accompanying the further increase in μ_e to 1.7×10^4 for the 2 %Si alloy and 1.4×10^4 for the 4 %Si alloy. These results indicate that the zero magnetostrictive alloys possess the good soft magnetic properties of $\lambda_s \fallingdotseq 0$, Bs>1.5 T and $\mu_e>10^4$. We further examined the changes in λ_s, Bs and μ_e with Ta for the zero magnetostrictive Fe-Zr-B-Al and Fe-Zr-B-Si alloys. As shown for the $Fe_{89}Zr_7B_2Al_2$ and $Fe_{88}Zr_7B_3Al_2$ alloys in Fig. 6, the nearly zero λ_s as well as high Bs above 1.5 T and high μ_e above 10^4 is obtained in a wide Ta interval of about 150 K, where the structure consists of bcc-Fe and remaining amorphous phases. In comparison with the data on λ_s(Ta) of the nanoscale bcc $Fe_{90}Zr_7B_3$ alloy shown in Fig. 2, it is to be noticed that the Ta range where the good soft magnetic properties are obtained is much wider than that (≡20 K)[8] for the Fe-Zr-B ternary alloy. The extension of the Ta interval is extremely important for future development as an engineering material. The similar extension of the Ta range where the good soft magnetic properties of $\lambda_s \fallingdotseq 0$, Bs>1.5 T and $\mu_e>10^4$ are obtained is also recognized for the nanoscale bcc $Fe_{87}Zr_7B_2Si_4$ and $Fe_{86}Zr_7B_3Si_4$ alloys. However, the optimum Ta interval for the Fe-Zr-B-Si alloys is about 120 K which is slightly smaller than that for the Fe-Zr-B-Al alloys.

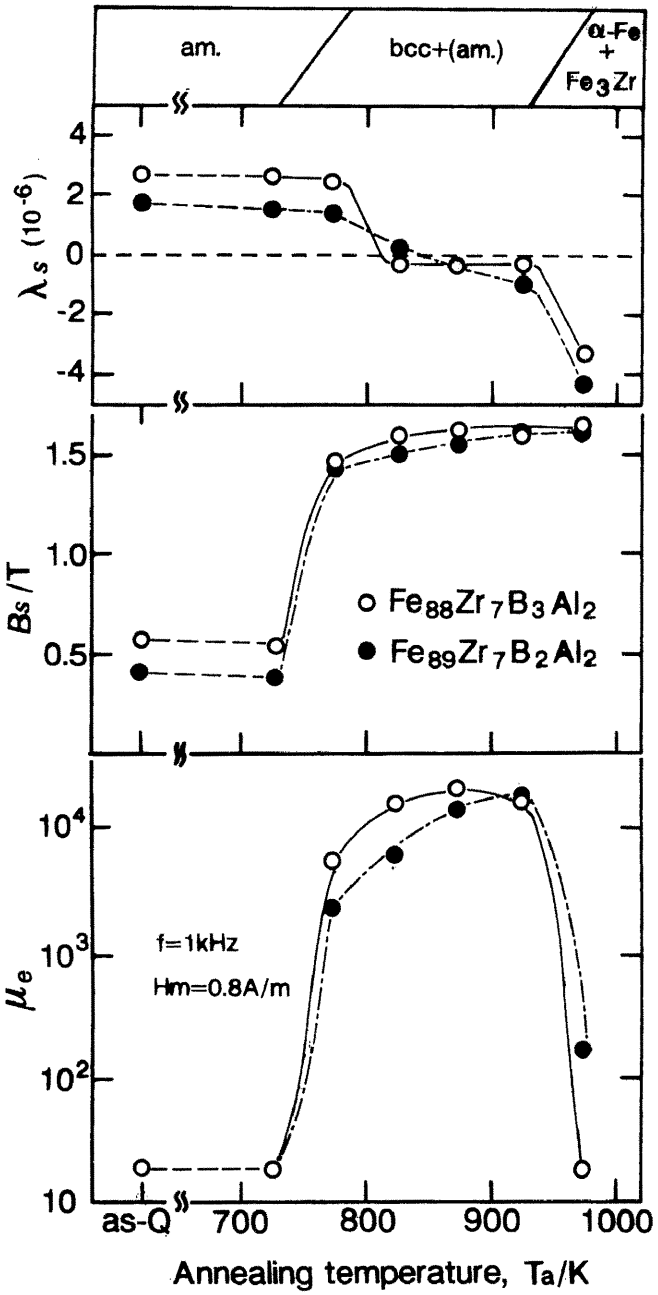

Fig. 6 Changes in the structure, λ_s, Bs and μ_e with Ta for the nanocrystalline $Fe_{89}Zr_7B_2Al_2$ and $Fe_{88}Zr_7B_3Al_2$ alloys.

The dissolution of Al or Si into the bcc-Fe phase was examined by using high-resolution TEM and nanobeam EDXS techniques. Figure 7 shows the high-resolution TEM image and the nanobeam electron diffraction pattern taken from the small region with a diameter of 5 nm for the $Fe_{88}Zr_7B_3Al_2$ alloy annealed for 3.6 ks at 873 K. It is seen that bcc particles with a particle size of 10 to 15 nm are embedded in an amorphous matrix. The EDXS profiles taken from the bcc-Fe phase and remaining amorphous phases indicate that the Al concentration in the bcc-Fe phase is about 2.6 %Al which is two times higher than that for the remaining amorphous phase. The Al element is enriched into the bcc-Fe phase. On the contrary, the Zr element is 4.1 at% for the bcc-Fe phase and 12.2 at% for the remaining amorphous phase, being significantly enriched into the remaining amorphous phase. As is the case with the Al element, the Si element in the $Fe_{86}Zr_7B_3Al_4$ alloy annealed for 3.6 ks at 873 K has also been recognized to be enriched into the bcc-Fe phase.

Here, it is important to summarize the advantages of the quaternary Fe-Zr-B-Al and Fe-Zr-B-Si soft magnetic alloys

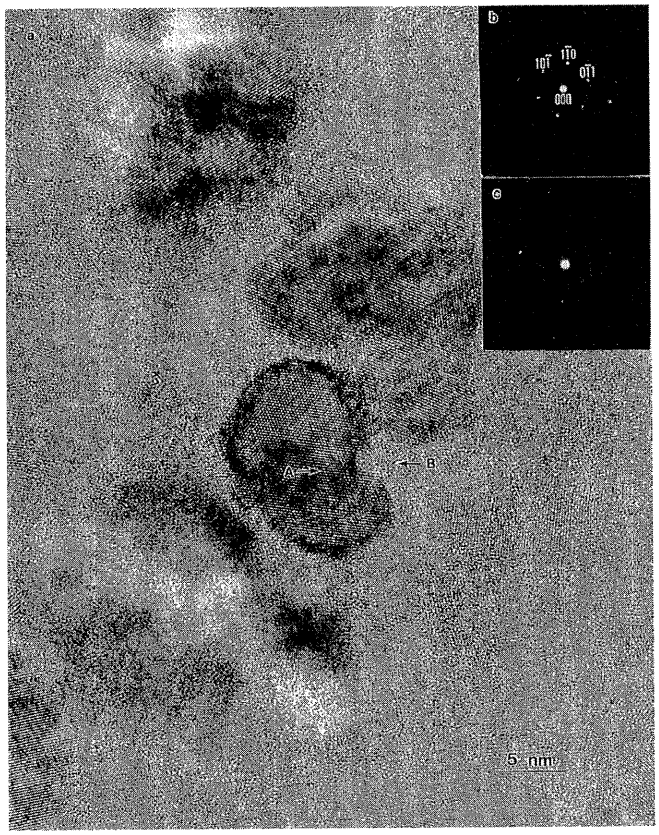

Fig. 7 High-resolution TEM image (a) and nanobeam electron diffraction patterns (b) and (c) taken from the small regions A and B, respectively, with a diameter of 5 nm for the nanocrystalline $Fe_{88}Zr_7B_3Al_2$ alloy.

consisting of nanoscale bcc particles embedded in the remaining amorphous phase, in comparison with those for the nanoscale bcc Fe-Zr-B ternary soft magnetic alloys. One can list up the following four points; (1) the achievement of zero λ_s in the wider Ta interval of 120 to 150 K, (2) the improvement of μ_e from 1.0×10^4 for the $Fe_{90}Zr_7B_3$ ribbon sample with a cross section of 0.015x1.5 mm^2 to 1.7×10^4 for the $Fe_{88}Zr_7B_3Al_2$ ribbon with the same sample morphology, (3) the achievement of the good soft magnetic properties of $\mu_e>10^4$ and Bs>1.5 T in the wider Ta interval of about 150 K, and (4) the increase in the maximum sample thickness for glass formation from about 20 μm for the $Fe_{90}Zr_7B_3$ alloy to about 30 μm for the $Fe_{86}Zr_7B_3Si_4$ alloy. From these advantages which cannot be obtained for the Fe-M-B ternary alloys, it is believed that the present new quaternary soft magnetic alloys will find some applications in the near future.

3. Distribution of B Element in the Nanoscale bcc Structure

As described in the previous section, the Al and Si elements are enriched into the bcc phase while the Zr element is segregated to the remaining amorphous phase. However, there has been no information on the distribution of B in the duplex nanostructure consisting of bcc-Fe and amorphous phases. We tried to analyze the distribution of B in the nanocrystalline $Fe_{90}Zr_7B_3$ alloy by using the atom-probe field ion microscopy (FIM) technique. Figure 8 (a) shows the change in the number of the detected ions for Fe, Zr and B elements in the as-quenched amorphous phase. No appreciable segregation is seen over the entire region, indicating that all the constituent elements are distributed homogeneously in the as-quenched amorphous phase. Furthermore, the concentrations of Fe, Zr and B determined by the atom-probe FIM method are just the same as those for the nominal concentrations. When the sample is heated to the temperature (823 K) just above the first exothermic peak, the structure changes to the nanocrystalline structure consisting of nanoscale bcc particles with a particle size of about 20 nm surrounded by the remaining amorphous phase, as shown in Fig. 9. In the nanophase structure, the change in the numbers of detected ions across the interface between bcc-Fe and amorphous phases is shown in Fig. 10 (a). Although the change near the interface is very slight for Fe, the change in the numbers of detected Zr and B ions is more

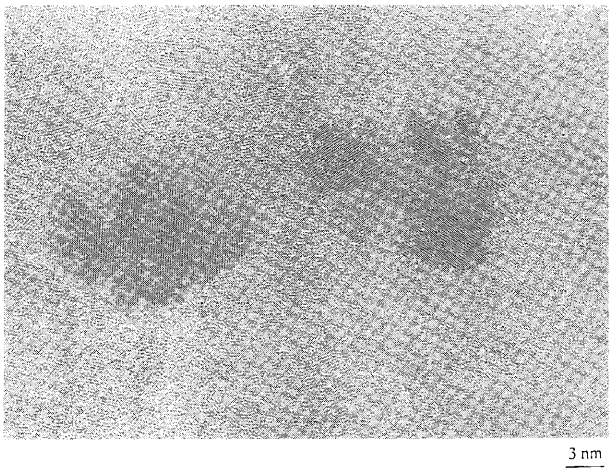

Fig. 9 High-resolution TEM image of the nanocrystalline $Fe_{90}Zr_7B_3$ alloy obtained by annealing for 600 s at 823 K.

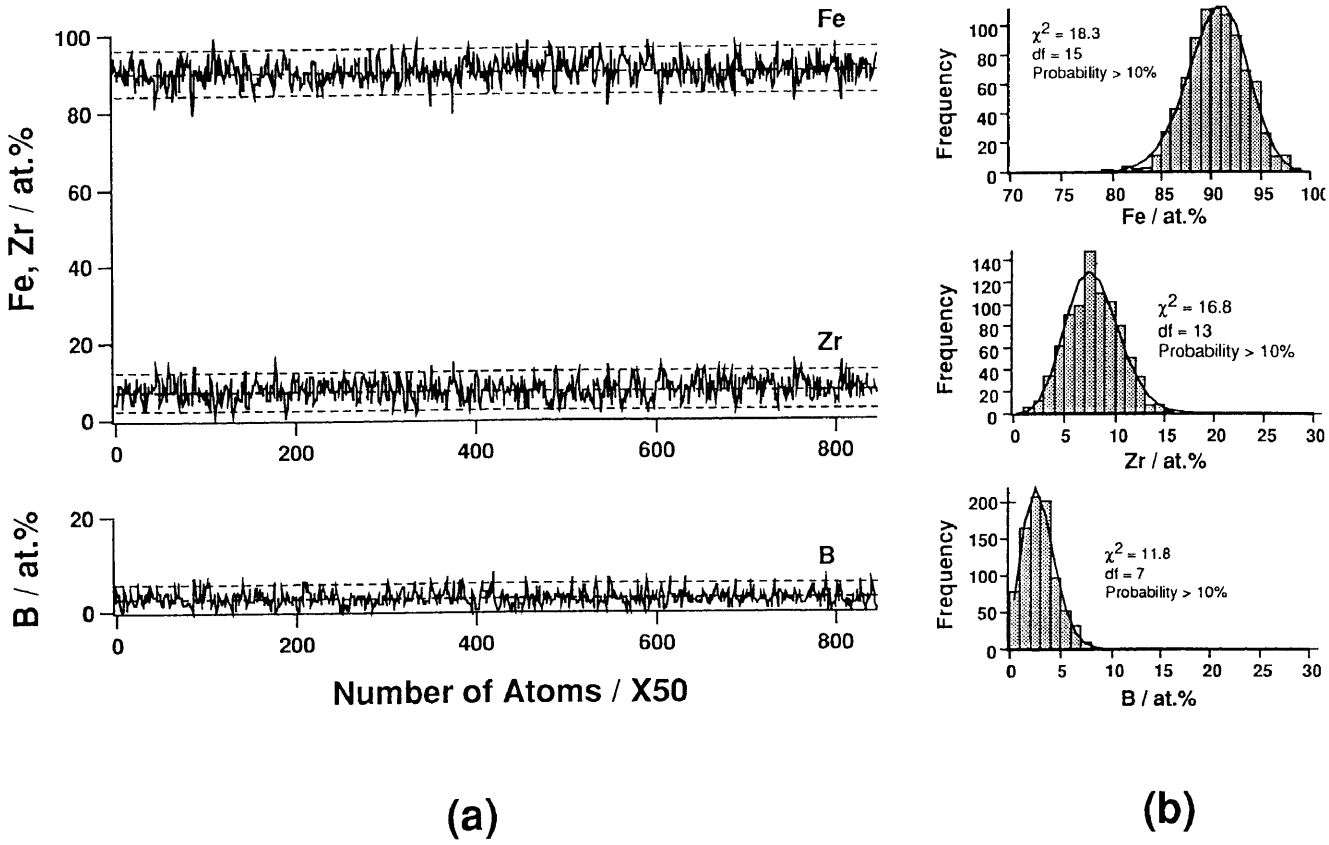

Fig. 8 (a) Atomic fractions of Fe, Zr and B atoms in the total numbers of detected atoms, and (b) frequency of their atomic fraction values for an as-quenched amorphous $Fe_{90}Zr_7B_3$ alloy.

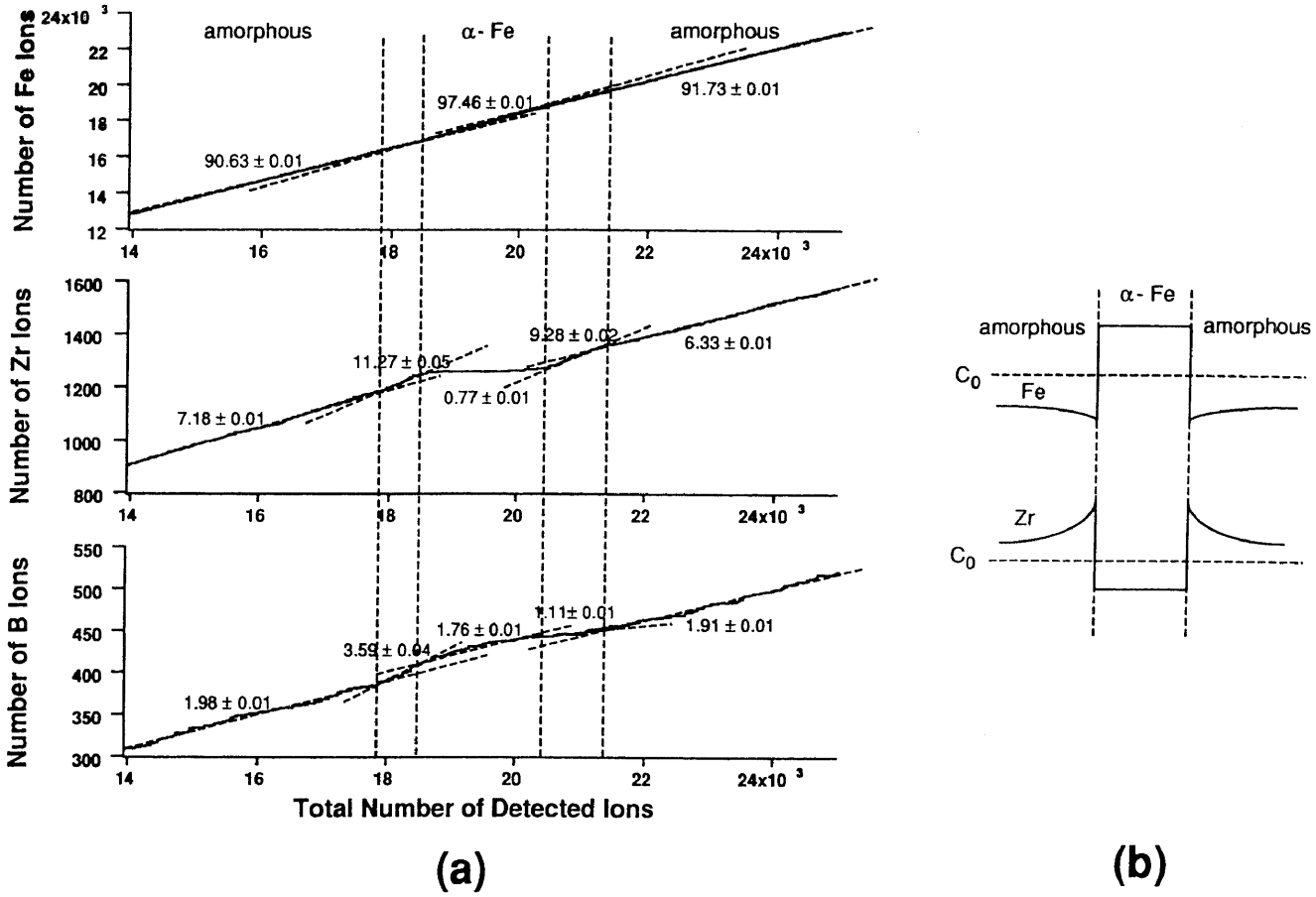

Fig. 10 (a) Fractions of the numbers of Fe, Zr and B ions in the total numbers of detected ions and concentration profiles of Fe and Zr elements in the region across the interface between amorphous and bcc-Fe phases for the amorphous $Fe_{90}Zr_7B_3$ alloy annealed for 600 s at 823 K.

significant, indicating that the concentrations of the Zr and B elements differ significantly near the interface between the bcc-Fe and amorphous phases. Figure 10 (b) shows the illustration of the concentration profiles of the Fe and Zr elements near the interface on the basis of the results shown in Fig. 10 (a). It is seen that the bcc-Fe phase has much higher Fe and much lower Zr concentrations as compared with their nominal concentrations, while the remaining amorphous phase has much lower Fe and much higher Zr concentrations. Furthermore, it is to be noticed that the Zr element is significantly enriched in the amorphous phase just near the interface and has a steep concentration gradient. The significant enrichment of Zr element in the remaining amorphous phase near the interface seems to play a dominant role in the achievement of the nanoscale bcc structure.

In order to investigate the distribution of the B element near the interface, the detailed result on the change in the number of the detected B element is shown in Fig. 11, where the result on the Zr element is also presented for comparison. One can notice the significant difference in the distribution behavior between B and Zr elements. That is, the change in the slope for B takes place continuously across the interface between bcc-Fe and remaining amorphous phases, while the change for Zr takes place only in the remaining amorphous phase. Based on the result, the concentration profiles of Fe, Zr and B elements are shown in Fig. 12. The B concentration is the lowest in the central

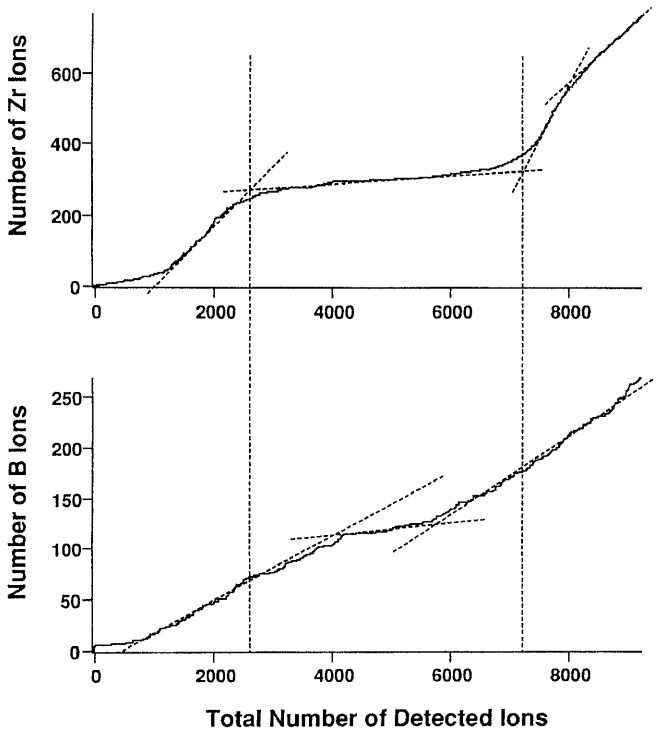

Fig. 11 Fractions of the numbers of Zr and B ions in the total numbers of detected ions in the vicinity of the interface between amorphous and bcc-Fe phases for the amorphous $Fe_{90}Zr_7B_3$ alloy annealed for 3.6 ks at 923 K.

region of the bcc-Fe phase, increases with approaching interface and shows a maximum value near the interface. With further moving to the inner region in the remaining amorphous phase region, the B concentration tends to decrease slightly. The maximum phenomenon of B near the interface seems to result from the enrichment of Zr at the interface because of the strongly attractive interaction between Zr and B atoms. Figure 13 also shows the analytical solute concentrations in the bcc phase for the nanoscale $Fe_{90}Zr_7B_3$ alloy subjected to an optimum annealing treatment. It is to be noticed that the B concentration is about 2 at% which is comparable to the nominal concentration (3 at%B). Furthermore, as shown in

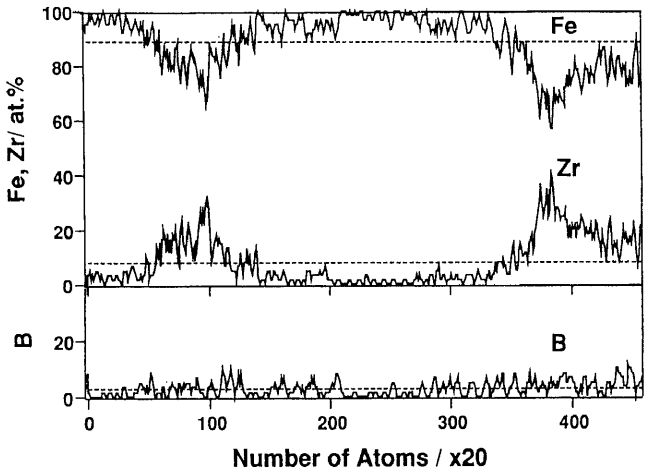

Fig. 12 Atomic fractions of the numbers of Fe, Zr and B atoms in the total number of detected atoms for the amorphous $Fe_{90}Zr_7B_3$ alloy annealed for 3.6 ks at 923 K.

Fig. 13(a), the concentration fluctuation of the B element is not significant as compared with those for Fe and Zr. The existence of the relatively high B content in the nanoscale bcc phase is presumably due to the strong interaction between Fe and B. Based on the above-described data obtained by the nanobeam EDXS analyses as well as by the atom-probe field ion microscopy, the concentration profiles of the constituent elements near the interface between bcc-Fe and remaining amorphous phases in the nanocrystalline bcc $Fe_{90}Zr_7B_3$, $Fe_{88}Zr_7B_3Al_2$ and $Fe_{86}Zr_7B_3Si_4$ alloys are shown in Fig. 14, along with the data of the nanocrystalline $Al_{89}Ni_8Ce_3$ alloy consisting of fcc-Al particles embedded in an amorphous matrix. It is clearly confirmed that the Zr and B elements are significantly enriched at the interface between bcc-Fe and amorphous phases. Consequently, the enrichment is concluded to be the origin for the achievement of the nanocrystalline bcc structure through the suppression of grain growth of the nanoscale bcc particles. The Ce element in the Al-Ni-Ce alloy also has the same important role in the formation of the nanoscale fcc-Al particles in coexistence with the remaining amorphous phase.

Here, it is important to discuss the criterion for the solute element which causes the appearance of the nanoscale mixed structure through the steep concentration gradient. The previous data indicate that the effective solute elements satisfy the following four criteria; (1) high melting temperature, (2) larger atomic size or larger atomic size ratio among the constituent elements. (3) large negative heat of mixing against the major element, and (4) nearly zero solubility limit against the major element. Furthermore, the reason why the remaining amorphous phase containing

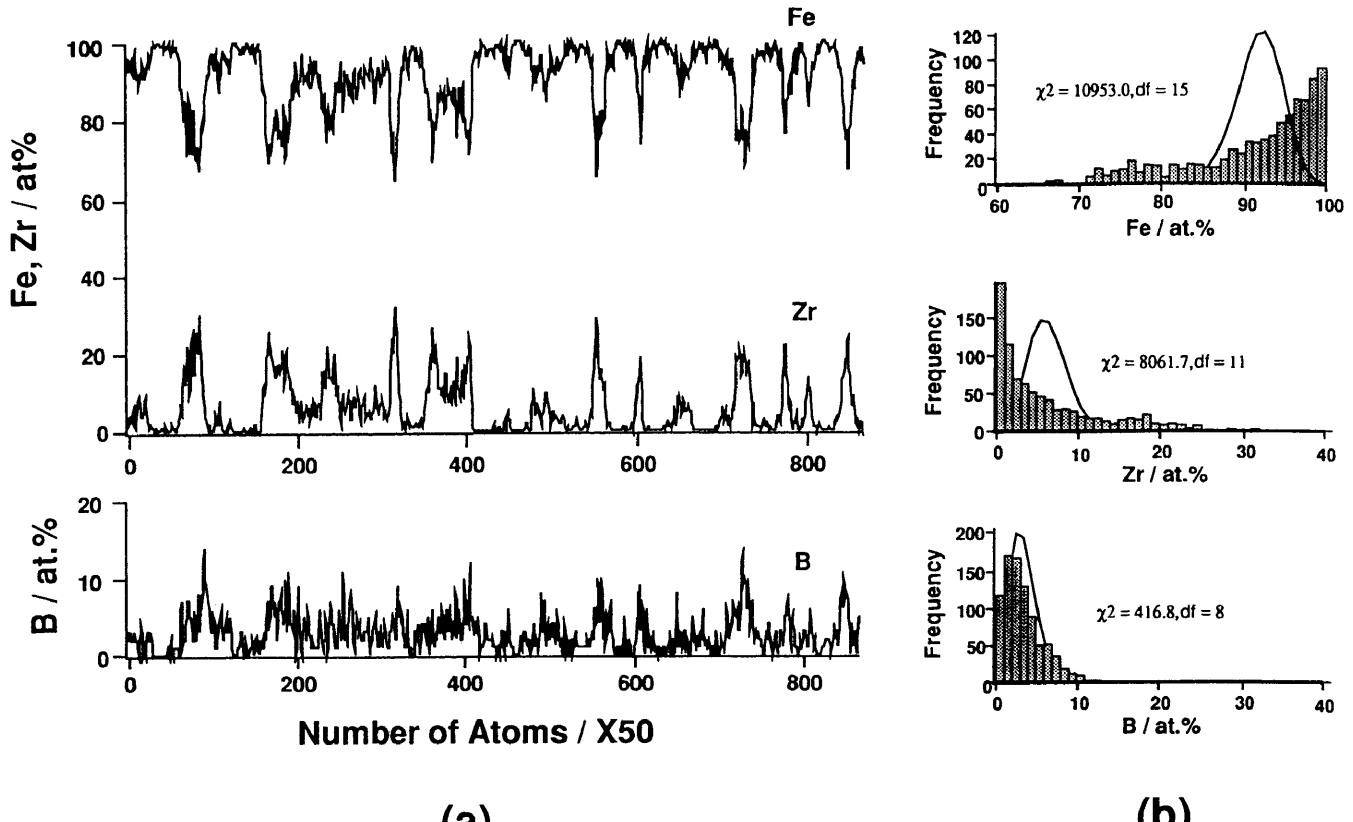

Fig. 13 (a) Atomic fractions of Fe, Zr and B atoms in the total number of detected atoms, and (b) frequency of their atomic fractions for the amorphous $Fe_{90}Zr_7B_3$ alloy annealed for 3.6 ks at 923 K.

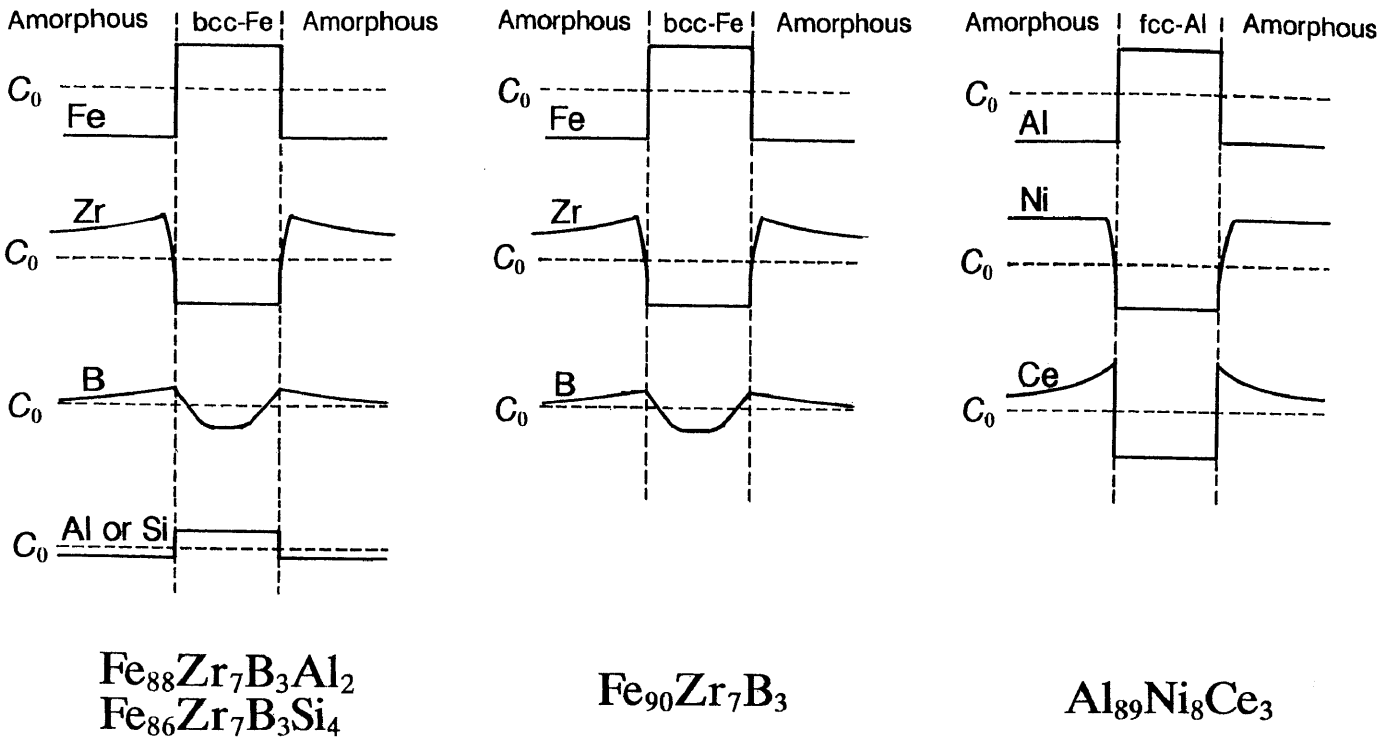

Fig. 14 Schematic illustration of the concentration profiles for the constituent elements in the nanocrystalline $Fe_{90}Zr_7B_3$, $Fe_{88}Zr_7B_3Al_2$ and $Fe_{86}Zr_7B_3Si_4$ alloys. The data on the nanocrystalline $Al_{89}Ni_8Ce_3$ alloy are also shown for reference.

the elements with the above-described four criteria can have the high thermal stability leading to the nanostructure is presumably due to the combination of the following four effects[9]; (1) high gradient effect leading to the increase in thermal stability of an amorphous phase, (2) suppression of grain growth leading to the homogeneous dispersion of nanocrystalline particles, (3) suppression of heterogeneous nucleation at the interface between crystalline particle and amorphous matrix, and (4) gradual progress of redistribution of alloy components among the constituent phases.

4. Nanocrystalline Hard Magnetic Alloys in Fe-rich Fe-Nd-B System[5,9,10]

It has previously been clarified by using the atom-probe FIM technique that the B element in the nanocrystalline bcc Fe-Zr-B alloy is enriched at the interface between bcc-Fe and remaining amorphous phases[11]. However, no precipitation of any boride resulting from the enrichment has been observed even at the interface in the Fe-Zr-B alloy annealed at higher temperatures. If one can find a more appropriate alloy system in which a ternary Fe-M-B boride precipitates preferentially at the interface through the enrichment effect of B element, it is expected that a new triplex nanostructure consisting of bcc-Fe, Fe-M-B boride and remaining amorphous phase is formed in an appropriate annealing state and leads to new functional properties which have not been obtained for duplex nanostructures. As one of the appropriate alloy systems, great attention was paid to Fe-rich Fe-Nd-B alloys. According to the previous data on the glass formation in the Fe-Nd-B system by melt spinning[12], the glass formation range is limited to the composition range below 87 at% Fe and no amorphous phase is formed at a high Fe concentration of 90 at%. Based on the similarity in alloy composition between $Fe_{90}Zr_7B_3$ and $Fe_{90}Nd_7B_3$, the possibility of forming an amorphous phase was examined in the composition range above 87 at% Fe. As a result, it has been confirmed that an amorphous phase is formed in the Fe-rich composition range between 87 and 90 at% Fe. No distinct contrast revealing the precipitation of a crystalline phase is seen in the bright-field electron micrographs of these Fe-rich alloys and the electron diffraction patterns also consist only of halo rings, indicating the formation of an amorphous phase.

The crystallization behavior of the Fe-rich Fe-Nd-B amorphous alloys was examined by DSC and TEM. Figure 15 shows the DSC curves of the amorphous $Fe_{90}Nd_7B_3$, $Fe_{89}Nd_7B_4$ and $Fe_{88}Nd_7B_5$ alloys. Three exothermic peaks marked with A, B and C are seen on the DSC curves of all the alloys, indicating that these Fe-rich amorphous alloys crystallize through three stages. In order to examine the crystalline phases corresponding to the three exothermic peaks, the X-ray diffraction patterns of the samples heated to the temperatures A, B and C are shown in Fig. 16. As indexed in the figure, the X-ray diffraction peaks are identified to be a bcc-Fe for the sample heated at 723 K, bcc-Fe and bct Fe_3B phases for the sample heated at 793 K and bcc-Fe and tetragonal $Fe_{14}Nd_2B$ phases for the sample heated at 923 K. It is therefore said that the three exothermic peaks correspond to the precipitation of bcc-Fe, Fe_3B and $Fe_{14}Nd_2B$ phases, respectively. The bright-field image of the $Fe_{90}Nd_7B_3$ alloy heated for 180 s at 923 K reveals that the annealed alloy consists of a very fine mixed structure with a grain size of about 20 nm. In the

corresponding electron diffraction pattern, a weak halo ring can be seen, in addition to the reflection rings corresponding to the bcc-Fe phase. This metallographic result indicates that the amorphous phase is remained even for the sample heated up to the third exothermic peak. Furthermore, the dark-field image taken from a part of the reflection rings of the bcc-Fe phase also reveals that the bcc phase consists of nanograins with a diameter of about 20 nm.

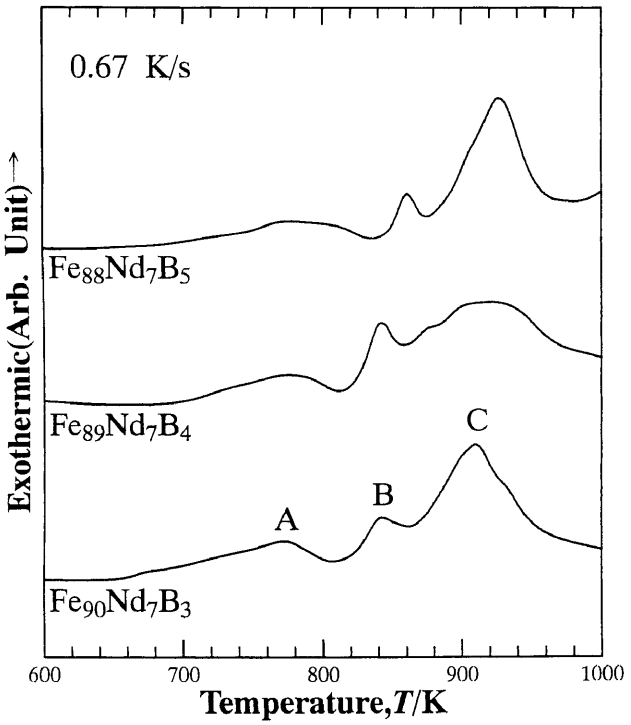

Fig. 15 DSC curves of the amorphous $Fe_{90}Nd_7B_3$, $Fe_{89}Nd_7B_4$ and $Fe_{88}Nd_7B_5$ alloys.

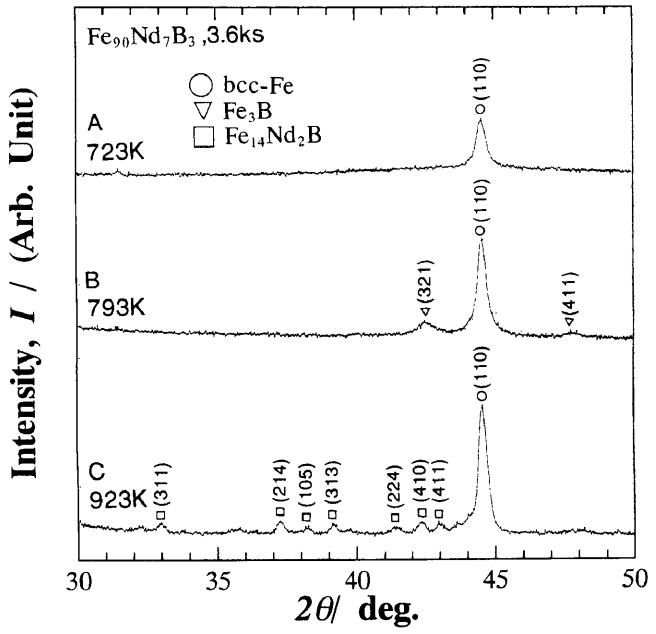

Fig. 16 X-ray diffraction patterns of the amorphous $Fe_{90}Nd_7B_3$ alloy annealed for 3.6 ks at 723 K, 793 K and 923 K corresponding to A, B and C, respectively on the DSC curve shown in Fig. 15.

The hysteresis J-H loop characteristics were examined for the nanocrystalline $Fe_{90}Nd_7B_3$, $Fe_{89}Nd_7B_4$ and $Fe_{88}Nd_8B_4$ alloys annealed at the temperatures around the third exothermic peak for various times. All these nanocrystalline alloys subjected to optimum annealing treatments possess smooth J-H loops exhibiting the simultaneous achievement of high remanence (Jr) of about 1.3 T and high coercive force (iHc) of about 260 kA/m and no appreciable step is seen in spite of the mixed structure alloys. Based on these hysteresis J-H loops, the Jr, iHc and maximum energy product $(BH)_{max}$ of the nanocrystalline $Fe_{89}Nd_7B_4$ and $Fe_{88}Nd_8B_4$ alloys are plotted as a function of annealing time (ta) at Ta=923 K in Fig. 17. It is to be noticed that the $Fe_{89}Nd_7B_4$ alloy annealed for 300 s at 923 K exhibits simultaneously high Br of 1.3 T, high iHc of 260 kA/m and high $(BH)_{max}$ of 146 kJ/m^3. The deviation from the optimum annealing treatment causes the significant degradation of the hard magnetic properties.

With the aim of investigating the reason for the appearance of the rather good hard magnetic properties, the nanocrystalline structure of the optimally annealed samples was examined by the high-resolution TEM technique. As an example, Fig. 18 shows the high-resolution TEM image (a) and the corresponding nanobeam electron diffraction patterns (b) to (f) taken from the particles B to F, respectively, in (a). As identified in Fig. 18 (b) to (f), the particles shown in Fig. 18 (a) are identified to be bcc-Fe for the B, C, E and F particles and tetragonal $Fe_{14}Nd_2B$ for the D particle. Thus, the nanocrystalline structure consists of bcc-Fe particles with a size of about 20 nm and $Fe_{14}Nd_2B$

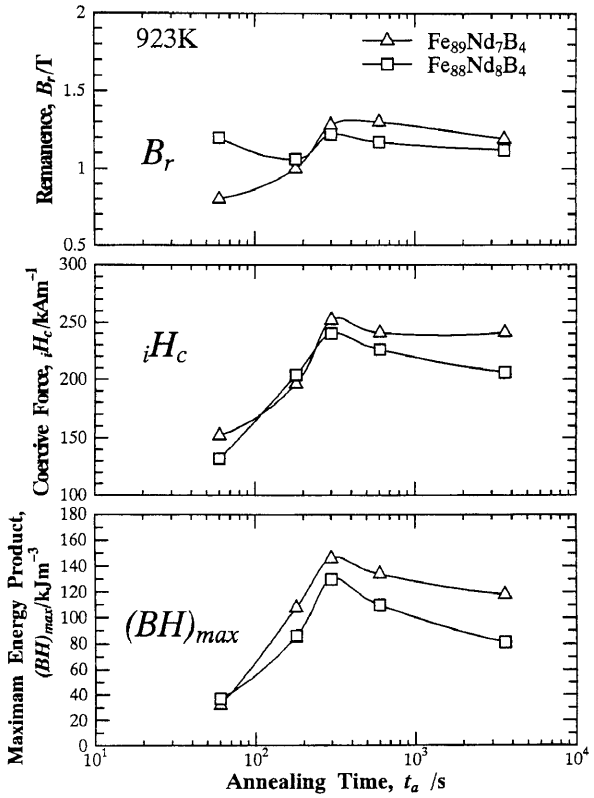

Fig. 17 Br, iHc and $(BH)_{max}$ as a function of annealing time for the $Fe_{89}Nd_7B_4$ and $Fe_{88}Nd_8B_4$ alloys annealed at 923 K.

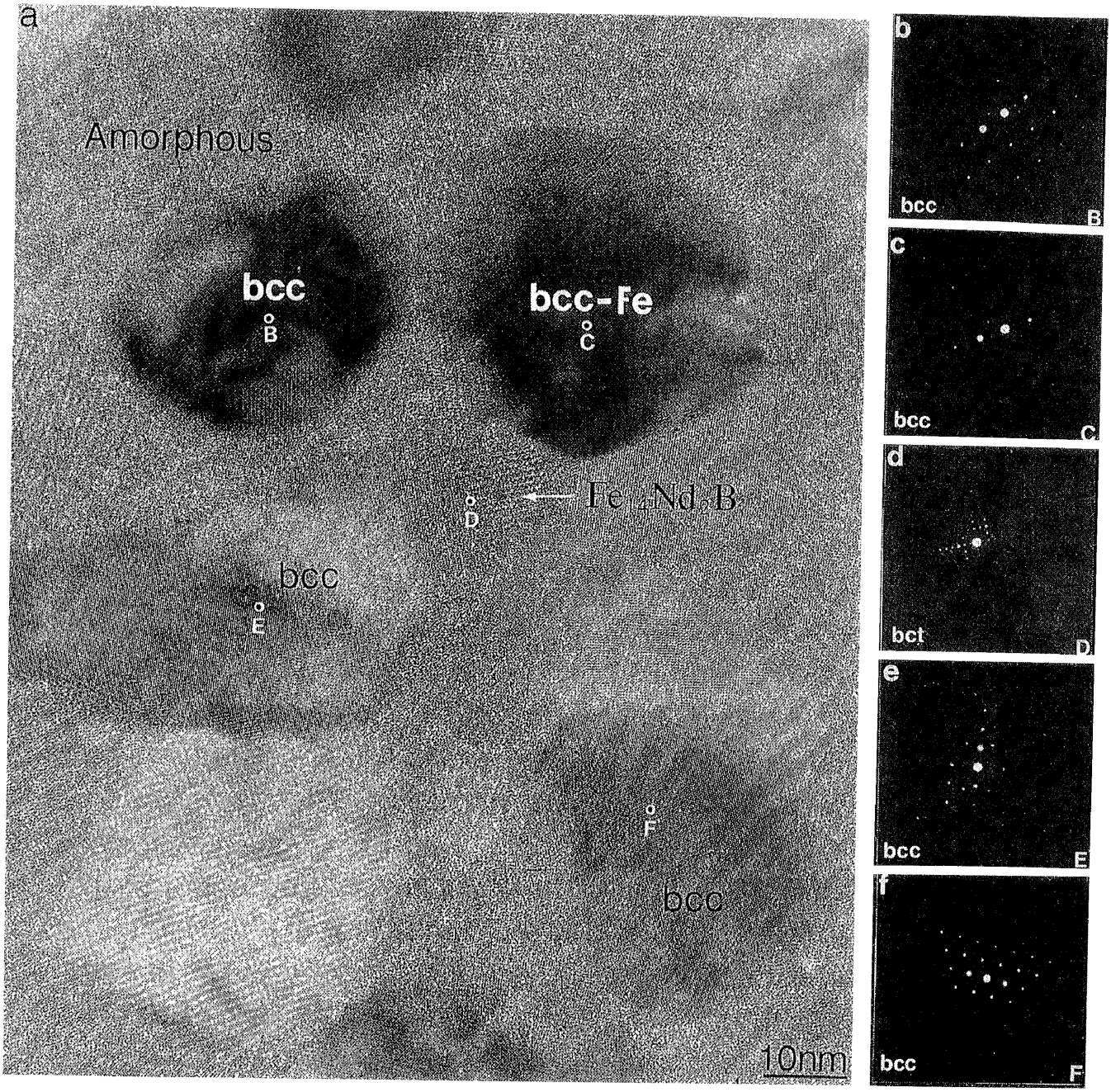

Fig. 18 High-resolution TEM image (a) of the $Fe_{90}Nd_7B_3$ alloy annealed for 60 s at 1023 K and nanobeam electron diffraction patterns (b) to (f) taken from the small regions B, C, D, E and F, respectively, with a diameter of 1 nm in (a).

particles with a size of about 15 nm. Furthermore, the nanoscale bcc-Fe and $Fe_{14}Nd_2B$ particles are surrounded by the remaining amorphous phase with a thickness of 5 to 10 nm. The interparticle spacing is measured to be about 5 to 10 nm between bcc-Fe and bcc-Fe particles and about 30 to 40 nm between tetragonal $Fe_{14}Nd_2B$ and $Fe_{14}Nd_2B$ particles. Consequently, the annealed $Fe_{90}Nd_7B_3$ alloy exhibiting rather good hard magnetic properties consists of the three phases of bcc-Fe, tetragonal $Fe_{14}Nd_2B$ and remaining amorphous phases. We also try to determine the solute concentration among the constituent phases. Figure 19 shows the high-resolution TEM image (a) and the EDXS profiles (b) and (c) taken from the regions A and B in (a), respectively, for the $Fe_{90}Nd_7B_3$ alloy annealed for 60 s at 1023 K. The analytical Nd content is about 0.5 at% for the bcc-Fe phase and about 14 at% for the $Fe_{14}Nd_2B$ phase. The Nd content in the remaining amorphous phase is about twice as high as the nominal Nd content, indicating that the Nd element is significantly enriched into the remaining amorphous phase. The distribution of B in the nanocrystalline Fe-Nd-B alloys was not determined, but the similarity in the alloy composition between the Fe-Zr-B[11] and Fe-Nd-B alloys allows us to presume the similar enrichment of B and Nd elements at the interface between bcc-Fe and remaining amorphous phases in the nanocrystalline Fe-Nd-B alloy, as illustrated in Fig. 20. The enrichment of the Nd and B elements near the interface seems to be the origin for the formation of the nanoscale mixed structure. Figure 21 summarizes the crystallization process of the Fe-rich Fe-Nd-B alloys. Although the

precipitation of the Fe_3B phase is not confirmed by TEM, the enrichment of B at the interface between bcc-Fe and amorphous phases causes the preferential precipitation of Fe_3B at the interface and the existence of the Fe_3B phase as an intermediate phase is thought to enable the precipitation of the $Fe_{14}Nd_2B$ phase through the enrichment of B in the pre-existing Fe_3B phase region. At any event, the maximum hard magnetic properties are obtained at the third stage consisting of the bcc-Fe, $Fe_{14}Nd_2B$ and remaining amorphous phases. The disappearance of the remaining amorphous phase with further increasing Ta causes the significant decrease in the hard magnetic properties through the drastic increase in the grain size of the bcc-Fe phase.

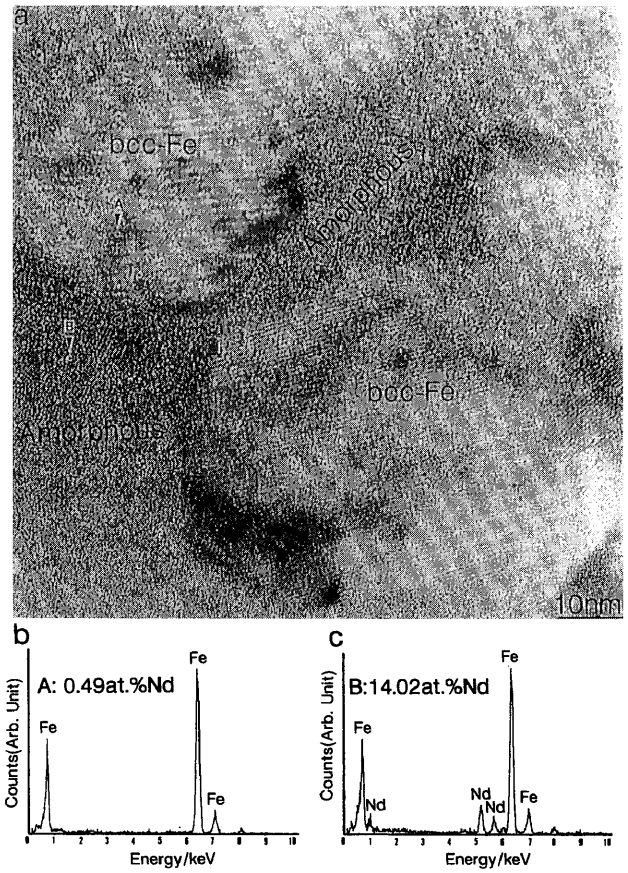

Fig. 19 High-resolution TEM image (a) of the $Fe_{90}Nd_7B_3$ alloy annealed for 60 s at 1023 K and EDXS profiles (b) and (c) taken from the small regions A and B, respectively, with a diameter of 1 nm in (a).

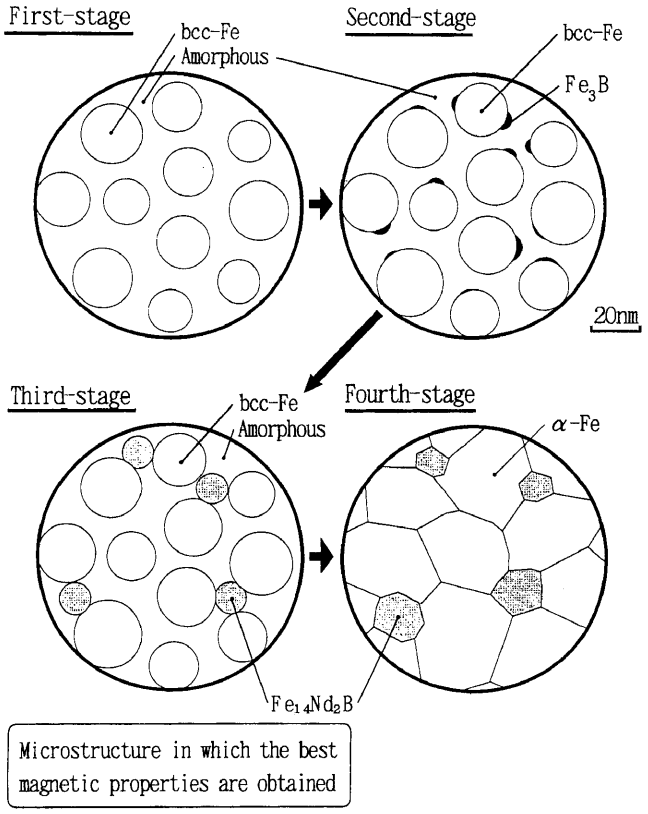

Fig. 21 Schematic illustration of the crystallization process for the amorphous $Fe_{90}Nd_7B_3$ alloy.

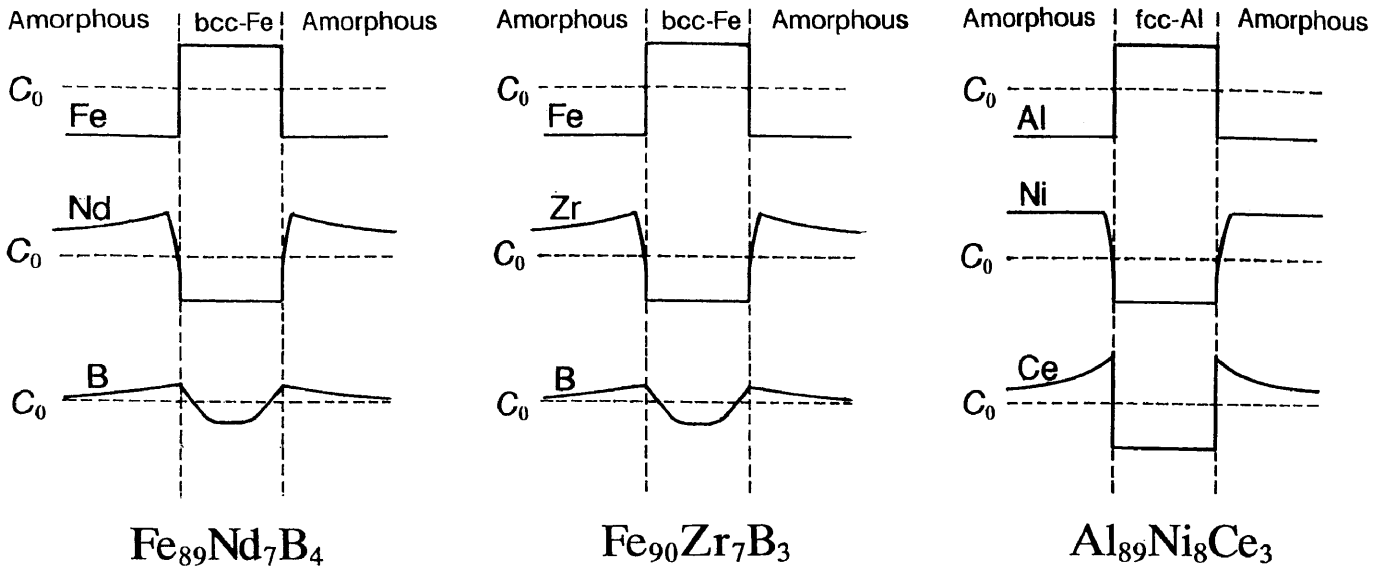

Fig. 20 Concentration profiles of Fe, Nd and B elements near the interface between amorphous and bcc-Fe phases for the nanocrys talline $Fe_{90}Nd_7B_3$ alloy. The data of the nanocrystalline $Fe_{90}Zr_7B_3$ and $Al_{89}Ni_8Ce_3$ alloys are also shown for reference.

5. Mechanism for the Appearance of Hard Magnetic Properties[5,9,10,13]

Here, it is important to investigate the mechanism for the appearance of the rather good hard magnetic properties for the present nanostructure alloys containing the intergranular amorphous phase. The appearance of the hard magnetic properties is thought to result from the exchange magnetic coupling mechanism among the ferromagnetic phases[14]. In the mechanism, the nucleation of the reversion of the magnetic domain walls generates in the central region of the soft magnetic bcc-Fe phase. When the mechanism is appropriate, the hard magnetic properties are significantly dependent on the grain size and volume fraction of the soft magnetic phase[15,16]. The previous theoretical relation indicates the following two important points; (1) the simultaneous achievement of high coercive force and high remanence is obtained for the nanoscale soft magnetic phase with a volume fraction of 40 to 50 %, (2) the high iHc cannot be obtained for the mixed phase alloys containing the soft magnetic phase above about 80 %, even though the grain size of the bcc phase is as small as about 10 nm. The volume fractions of the constituent phases for the present Fe-Nd-B alloys are about 60 % for the bcc-Fe phase, 20 % for the remaining amorphous phase and 20 % for the $Fe_{14}Nd_2B$ phase and hence the total volume fraction of the soft magnetic phases is roughly estimated to be 80 %, as illustrated in Fig. 22 (a). Even in the structural state containing the soft magnetic phase of about 80 % in volume fraction, the rather good hard magnetic properties have been obtained. In the structural state shown in Fig. 22(b) where the bcc phase occupies 80 % in volume fraction and has a large grain size, it is easy to understand that the nucleation of the reversion of magnetic domain walls takes place in the central region of the bcc-Fe soft magnetic phase. On the other hand, the coexistence of the finely mixed two phases in the soft magnetic phase field is presumed to act as an effective resistance against the nucleation of reversion of magnetic domain walls, leading to the increase in iHc. Furthermore, the intergranular amorphous phase with a thickness of 5 to 10 nm also can act as an effective exchange magnetic coupling medium between bcc-Fe and bcc-Fe or tetragonal $Fe_{14}Nd_2B$ phases, leading to the increase in remanence. Thus, the

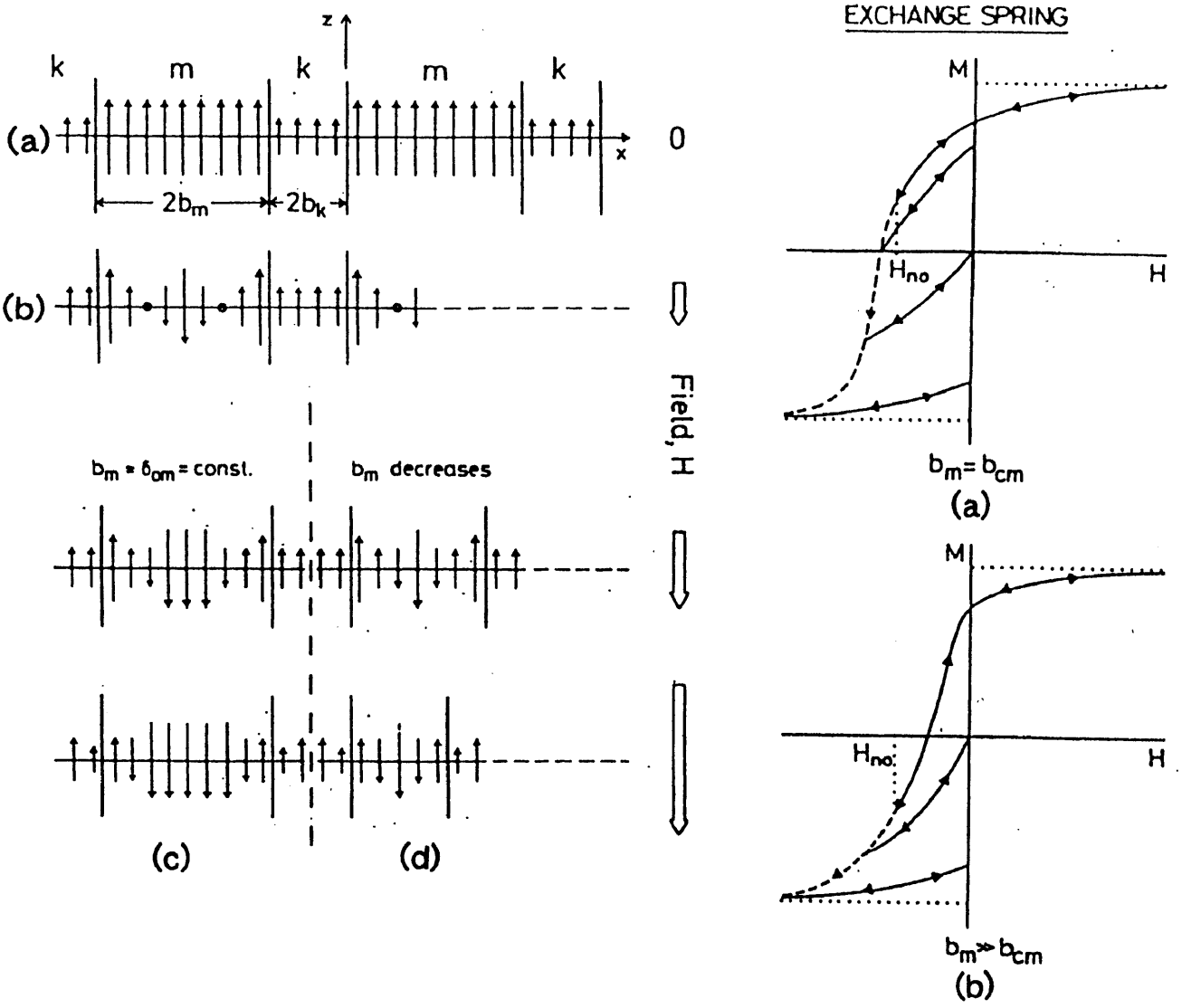

Fig. 22 Schematic illustration showing the change of the magnetic spin in the soft (m) and hard (k) magnetic phases with increasing applied field for the nanoscale mixed structure consisting of soft and hard magnetic phases. The data were taken from Ref. 14).

intergranular amorphous phase is thought to play a dominant role in the achievement of the good hard magnetic properties for the Fe-rich Fe-Nd-B alloys containing a high volume fraction of soft magnetic phases. It is therefore important to summarize the role of the intergranular amorphous phase for the nanocrystalline Fe-rich Fe-Nd-B alloys. In the new triplex nanostructure consisting of bcc-Fe with a particle size of about 20 nm, tetragonal $Fe_{14}Nd_2B$ with a particle size of about 15 nm and the remaining amorphous phase with a thickness of 5 to 10 nm, the intergranular amorphous network phase can act as an effective exchange magnetic coupling medium between bcc-Fe and bcc-Fe or tetragonal $Fe_{14}Nd_2B$ phases, leading to the achievement of high remanence. In addition, the existence of the intergranular amorphous network phase can suppress the reversion of magnetic domain walls in the central region of the soft magnetic phase, leading to the achievement of high iHc. This suppression is presumably because of the simultaneous achievement of the inhomogeniety of the constituent phases and solute concentrations, large concentration gradient at the interface and inhomogeniety of ferromagnetic properties for the bcc-Fe and remaining amorphous phases. Consequently, one can regard the present Fe-rich Fe-Nd-B hard magnetic alloys as a multiple exchange-coupling type magnet.

Figure 23 shows the Fe-rich composition range in which the high $(BH)_{max}$ values exceeding 100 kJ/m^3 are obtained in the present study. The composition range is significantly different from those for the commercial sintering type[18] and melt-quenching type magnets[19] marked with A and B, respectively. Table 2 summarizes the Br, iHc and $(BH)_{max}$ values for the present Fe-rich magnets containing intergranular amorphous phase, together with those for commercial permanent magnets. It is recognized that these characteristics are comparable to those for the $SmCo_5$ magnet[20]. Furthermore, the feature of the present permanent magnet is attributed to the high $(BH)_{max}$ values through the high Br.

Table 2 Comparison of the hard magnetic properties for the nanocrystalline Fe-rich Fe-Nd-B magnet containing an intergranular amorphous phase with those for conventional permanent magnets.

	Br (T)	iHc (kA/m)	$(BH)_{max}$ (kJ/m^3)
Ferrite Magnet	0.40	312	30
Alnico Magnet	0.90	112	42
$SmCo_5$ Magnet	0.89	1360	151
Sm_2Co_{17} Magnet	1.14	800	239
$Nd_2Fe_{14}B$ Magnet	1.31	999	319
Nanocrystalline $Fe_{89}Nd_7B_4$ Magnet with High Fe Concentration	1.30	252	146

It is finally important to point out the effect of quenching rate on the achievement of the rather good hard magnetic properties for the Fe-rich Fe-Nd-B alloys. With decreasing cooling rate, the structure of the melt-spun $Fe_{89}Nd_7B_4$ alloy changes from a mostly single amorphous phase to a mostly single bcc phase through coexistent amorphous plus bcc phases. The DSC curves also change in the order of three stages, two stages and a single stage with decreasing cooling rate. The resulting hysteresis J-H curve shows significant changes among the three samples even after the optimal annealing treatment, as shown in Fig. 24. The smooth J-H loop without appreciable step can be obtained only for the amorphous phase and the use of the amorphous plus bcc-Fe phases causes the J-H loop with a distinct step. Furthermore, no appreciable hard magnetic characteristics

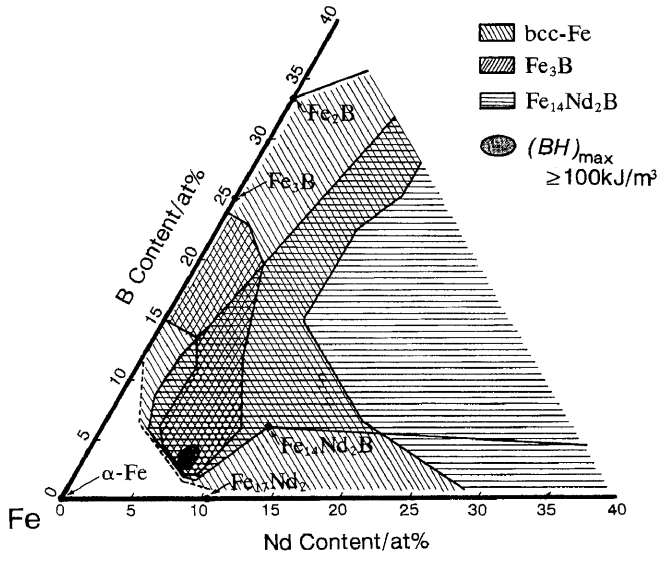

Fig. 23 Composition range in which the high $(BH)_{max}$ values above 100 kJ/m^3 are obtained for the nanocrystalline Fe-rich Fe-Nd-B alloys containing above 88 at%Fe. The data of the annealed phases taken from Ref.17) are also shown for reference.

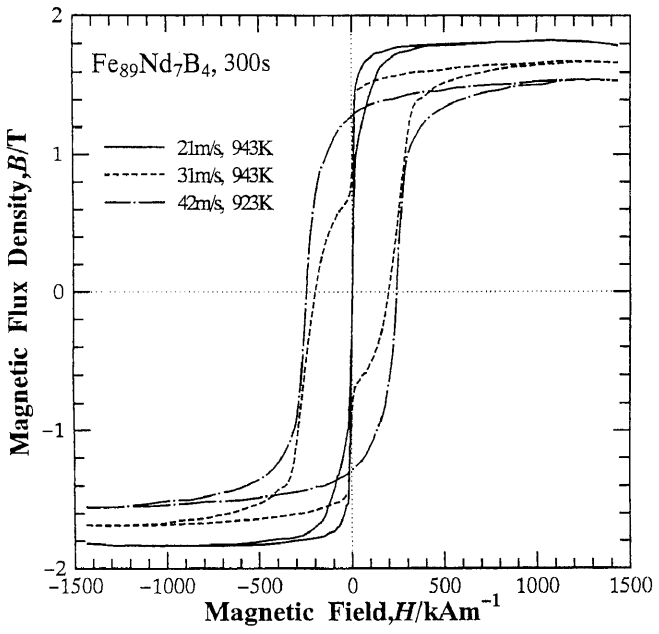

Fig. 24 Hysteresis J-H loops of melt-spun $Fe_{89}Nd_7B_4$ alloys annealed for 300 s at 923 and 943 K after the preparation at the circumferential velocities of 42, 31 and 21 m/s.

are not obtained for the mostly single bcc phase. It is therefore concluded that the rather good hard magnetic properties are obtained only in the use of the mostly single amorphous phase as a starting material. This result also indicates clearly the importance of the residual existence of the intergranular amorphous phase for the achievement of the rather good hard magnetic properties. Although some trials of preparing a hard magnetic alloy had previously been made for the Fe-rich Fe-Nd-B alloys containing about 90 at% Fe, no successful result leading to the J-H loop without appreciable step has been obtained. The present first success seems to be attributed to the use of the mostly single amorphous phase.

6. Conclusions

The further precise control in the solute concentration of the bcc-Fe phase by the use of Fe-Zr-B base alloys containing Al or Si was found to cause the further improvement of the soft magnetic properties as well as the remarkable extension of optimal annealing condition through the achievement of zero λ_s. Furthermore, by taking the enrichment of B element at the interface between bcc-Fe and remaining amorphous phases into consideration, we succeeded in fabricating the new triplex nanostructure consisting of bcc-Fe, tetragonal $Fe_{14}Nd_2B$ and remaining amorphous phases. The attainment of the new triplex nanostructure has enabled the appearance of good hard magnetic properties with the features of new Fe-rich compositions and new multiple type exchange coupling mechanism. These novel results allow us to expect that a new functional material can be synthesized through the combination of further precise nanostructure control and new alloy composition.

1) A. Inoue: Bulletin Japan Inst. Metals, **34** (1995) 934.
2) Nanostructured Materials, eds. Benard H. Kear, Richard W. Siegel and Thomas Tsakalakos , **6** (1995) p. 1 - 496.
3) Y. Yoshizawa, S. Oguma and K. Yamauchi: J. Appl. Phys. **64**(1988) 6044.
4) K. Suzuki, N. Kataoka, A. Inoue, A. Makino and T. Masumoto: Mater. Trans., JIM **31** (1990) 743.
5) A. Inoue, A. Takeuchi, A. Makino and T. Masumoto: Mater. Trans., JIM **36** (1995) 676.
6) A. Inoue, Y. Miyauchi and T. Masumoto: Mater. Trans., JIM **36** (1995) 689.
7) A. Inoue, Y. Miyauchi, A. Makino and T. Masumoto: Mater. Trans., JIM **37** (1996) 78.
8) K. Suzuki, A. Makino, N. Kataoka, A. Inoue and T. Masumoto: Mater. Trans., JIM **32** (1991) 93.
9) A. Inoue, A. Takeuchi, A. Makino and T. Masumoto: Mater. Trans., JIM **36** (1995) 962.
10) A. Inoue, A. Takeuchi, A. Makino and T. Masumoto: IEEE Trans. Magn. **MAG-31** (1995) 3626.
11) K. Hono, A. Inoue and T. Sakurai: Acta Met. to be submitted.
12) L.X. Liao and Z. Altounian: J. Appl. Phys. **66** (1989) 768.
13) A. Inoue: Int. Symp. on Metastable, Mechanically Alloyed and Nanocrystalline Materials (Quebec,1995) in press.
14) E.F. Kneller and R. Hawig: TEEE Trans. Magn. **MAG-27** (1991) 3588.
15) T. Schrefl, H. Kronmuller and J. Fidler: J. Magn. Magn Materials **127**(1993) L273.
16) T. Schrefl, R. Fischer, J. Fidler and H. Kronmuller: J. Appl. Phys. **76** (1994) 7053.
17) K. Nagayama, H. Ino and T. Umeda: J. Japan Inst. Metals **54** (1990) 720.
18) M. Sagawa, S. Fujimura, N. Togawa, H. Hamamoto and Y. Matsuura: J. Appl. Phys. **55** (1984) 2083.
19) J.J. Croat, J.F. Herbst, R.W. Lee and F.E. Pinkerton: J. Appl. Phys. **55** (1984) 2078.
20) J.D. Livingstone and M.D. McConnell: J. Appl. Phys. **43** (1972) 4756.